Scripta Materialia 226 (2023) 115210

Contents lists available at ScienceDirect

Scripta Materialia

journal homepage: www.journals.elsevier.com/scripta-materialia

The effect of plastic deformation on hydrogen diffusion in nickel Alloy 625

Xu Lu [a,*], Andrés Díaz [b,*], Jun Ma [a], Dong Wang [a], Jianying He [c], Zhiliang Zhang [c], Roy Johnsen [a]

[a] Department of Mechanical and Industrial Engineering (MTP), Norwegian University of Science and Technology (NTNU), Richard Birkelands vei 2B, Trondheim N-7491, Norway
[b] University of Burgos, Escuela Politécnica Superior, Avenida Cantabria s/n, Burgos 09006, Spain
[c] Department of Structural Engineering, Norwegian University of Science and Technology, Richard Birkelands vei 1A, Trondheim N-7491, Norway

ARTICLE INFO

Keywords:
Nickel alloy 625
Hydrogen
Diffusion
Plastic deformation
Permeation

ABSTRACT

Recently, several hydrogen-assisted failures have been reported on different nickel alloys used in the subsea oil and gas industries. It is thus essential to correlate hydrogen uptake and diffusion behavior with stress conditions for an in-depth understanding of the failures. This study reports the first-hand finding on hydrogen diffusion behavior in a nickel Alloy 625 under different pre-strain levels by combining the electrochemical permeation test and diffusion model, with a particular focus on the effect of grain boundary carbide. As the multiplication of dislocations was claimed to trap hydrogen atoms and reduce the diffusivity by increasing the strain levels from 0.05 to 0.2, an acceleration in hydrogen diffusivity was however observed when the strain was higher than 0.1. This phenomenon was deduced to be caused by the diffusion highways by the hydrogen-enhanced strain-induced vacancy formation at the grain boundaries and reduced hydrogen trapping by the fractured carbides.

Hydrogen embrittlement has been recognized as a critical problem for components used in the oil and gas industry. Specifically, for nickel alloys with prominent mechanical properties and excellent corrosion resistance, hydrogen-induced stress cracking was reported as the predominant factor for the unexpected failures after years of application [1–7]. The well-documented reason is the existence of secondary phases both in the matrix and at the grain boundaries. For precipitation-hardened nickel alloys, the high strength is typically achieved by γ' and γ'' strengthening phases formed in the matrix during aging processes. However, other secondary phases such as δ phase (Ni_3Nb), η phase (Ni_3Ti), σ phase/F phase and various carbides and carbonitrides can also be found based on the chemical compositions, processing, and heat treatments [8–11]. These secondary phases can be crack initiation sites under hydrogen occlusion causing either transgranular or intergranular fractures [7,12,13]. As a prominent controlling factor, hydrogen uptake and diffusion through the alloy matrix should be particularly emphasized amidst hydrogen embrittlement analysis. Typical investigations on hydrogen uptake and diffusion are focused on virgin materials without straining [14–21]. However, it has been reported that tensile stress in both the elastic and plastic regimes can significantly influence hydrogen transport [22–26]. On the one hand, these studies claimed an enhanced hydrogen diffusivity during elastic straining because of the lattice expansion such that the material can accommodate more hydrogen interstitially [27]. On the other hand, pronounced dislocation multiplications can trap hydrogen and retarded hydrogen diffusion if further strained into the plastic range [13,26,27]. However, most studies have been focused on body-centered structure steels, instead of widely used nickel alloys. Furthermore, no studies have investigated the effect of secondary phases on the hydrogen diffusion in the process of plastic deformation. Therefore, to complement the pioneering work, the synergistic effect of plastic deformation and grain boundary precipitate on hydrogen diffusion in a face-centered structure nickel Alloy 625 was explicitly investigated using the electrochemical permeation technique and hydrogen diffusion model, aiming to shed light on the plasticity-interplayed hydrogen embrittlement mechanisms of nickel alloys.

The nominal composition and heat treatment process for Alloy 625 was reported in [28]. The tensile specimens, with a gauge dimension of 3 × 16 × 32 mm (thickness × width × length), were machined from a bar. To investigate the effect of plastic deformation on hydrogen diffusivity, the specimens were pre-strained under uniaxial tension to three nominal strain levels (ε): *i.e.*, 0.05, 0.1 and 0.2, using the MTS Series 809 Test System at a strain rate of 10^{-3} s^{-1}. Afterwards, disk specimens used for electrochemical permeation tests were machined out of both the plastically deformed and the unloaded samples (Fig. 1). The disk samples were further ground until 4000 SiC grinding paper to a final

* Corresponding authors.
E-mail addresses: xu.lu@ntnu.no (X. Lu), adportugal@ubu.es (A. Díaz).

https://doi.org/10.1016/j.scriptamat.2022.115210
Received 10 November 2022; Received in revised form 24 November 2022; Accepted 25 November 2022
Available online 1 December 2022

thickness of 80 ± 10 μm. The electrochemical permeation test was conducted in a Devanathan−Stachursky two-component electrolytic permeability cell, where the sample was clamped between an oxidation cell and a charging cell. A detailed description of the setup has been documented in [28]. The electrolyte in the oxidation cell was 0.1 M NaOH, while 0.2 g/L thiourea was added to the charging cell to promote hydrogen adsorption. On the oxidation side, the sample was polarized to a constant potential of +300 mV vs. a saturated calomel electrode (SCE), and on the charging side, a constant cathodic current density of -20 mA/cm^2 was applied using a Gamry potentiostat. The permeation test was conducted at room temperature (295 K). In addition, the microstructure of the alloy was characterized using scanning electron microscopy (SEM) and energy dispersive spectroscopy (EDS). To quantify the dislocation density at different strain levels, scanning transmission electron microscopy (STEM) analysis was carried out on the focused ion beam (FIB)-milled lamellae, which has a final thickness of ~80 nm.

In contrast to ferrous alloys, hydrogen transport through nickel-based alloys involves a competition between the trapping and grain boundary short-circuit diffusion [14–21,29]. Because conventional trapping modelling, as in Sofronis and McMeeking [30], cannot directly capture the later phenomenon, the approach proposed by Turk et al. [31] was adopted to reproduce the grain boundary diffusion using an extra flux term. Two different trapping sites were modelled, and thus the total hydrogen was split into three populations: hydrogen concentration in lattice sites (C_L), in dislocations (C_d) and in grain boundaries (C_{gb}). Assuming thermodynamic equilibrium and a multi-trapping mass balance [32], the governing equation for hydrogen transport and the corresponding equilibrium terms can be expressed as follows:

$$\left(1+\frac{\partial C_d}{\partial C_L}+\frac{\partial C_{gb}}{\partial C_L}\right)\frac{\partial C_L}{\partial t}+\nabla\cdot\left[\left(D_L+D_{gb}\frac{\partial C_{gb}}{\partial C_L}\right)\nabla C_L\right]=0 \tag{1}$$

$$\frac{\partial C_d}{\partial C_L}=\frac{K_d N_d/N_L}{\left[1+C_L/N_L(K_d-1)\right]^2} \tag{2}$$

$$\frac{\partial C_{gb}}{\partial C_L}=\frac{K_{gb}N_{gb}/N_L}{\left[1+C_L/N_L\left(K_{gb}-1\right)\right]^2} \tag{3}$$

where D_L and D_{gb} represent the lattice diffusivity of hydrogen and the diffusivity of hydrogen along grain boundaries. The equilibrium constants depend on the corresponding trap binding energy, *i.e.*, $K_d = \exp[E_d/(RT)]$ and $K_{gb} = \exp[E_{gb}/(RT)]$, being R the gas constant and T the temperature (295 K). Both energies were taken as 26.04 kJ/mol and $D_L = 2.03\times10^{-7}$exp [-44.46 [kJ/mol]/(RT)] [28]. The number of lattice sites per unit volume, N_L, is defined as 9.15×10^{28} sites/m^3 assuming an usual nickel density (8.9 g/cm^3) and a preferred octahedral face-centered cubic occupancy [33]. On the other hand, trap densities were deduced from the experimental observations: the density of dislocation trapping sites, N_d, is expressed from the geometrical relationship with the dislocation density in Eq. (4) [34], which was measured through STEM bright field images using the line intercept method for each pre-strain level [35].

$$N_d=\sqrt{3}\rho/a \tag{4}$$

where a is the nickel lattice parameter (3.499×10^{-10} m). Similarly, a cubic grain shape is assumed to determine the number of grain boundary sites per unit volume, N_{gb}, as a function of the STEM-based measurements for the grain size ($d_g = 10$ μm) and the grain boundary thickness ($t_{gb} = 5$ nm) [31]:

$$N_{gb}=N_L\left(1-\frac{d_g^3}{\left(d_g+t_{gb}\right)^3}\right) \tag{5}$$

It must be noted that the extra flux term to account for grain boundary acceleration invalidates the assumption of a triangular C_L distribution at the steady-state, and therefore the steady-state flux j_{ss} does not only depend on the concentration on the entry side C_L^0. Solving the differential equation at the steady-state, the following equation can be obtained:

$$j_{ss}=\frac{C_L^0}{L}\left(D_L+D_{gb}\frac{K_{gb}N_{gb}/N_L}{1+C_L^0/N_L\left(K_{gb}-1\right)}\right) \tag{6}$$

Therefore, the C_L^0 boundary condition was deducted from the experimental j_{ss} and the assumed trapping values after solving the corresponding second-order equation. To assess the influence of grain boundary hydrogen acceleration, the permeation was numerically reproduced in a 1D model in the Comsol Multiphsics 6.0, which is suitable for the simulation of coupled phenomena and the *Transport of Diluted Species* module by implementing Eqs. (1) to (6). Different $D_{gb} = \phi D_L$ values were iterated until the fitted D_{eff} matches the experimental data, where ϕ represents a pre-factor.

Fig. 2(a) shows the pristine micrograph of Alloy 625 exhibiting a typical polycrystalline face-centered cubic structure with an average grain size of 10 μm. Grain boundary precipitates highlighted by the yellow arrows. EDS mapping on the area enclosed by the yellow box demonstrates that the precipitates are rich in C, Mo, Nb and deplete in Ni. A previous study reported the precipitate as M_6C carbide, which shares an incoherent interface with the matrix [28]. The initial carbide fraction was measured to be 0.67%, which equals to approximately 9.5% of the total grain boundary length. After the sample was strained to 0.05, cracks in the carbides started to form, as indicated by the red arrows (Fig. 2(f)). Upon further straining, more cracked carbides appeared (Fig. 2(g, h)). In addition, when the samples were being strained, the contrast change in the micrographs (Fig. 2(f)−(h)) indicates dislocation multiplication and interaction during the plastic deformation. The STEM images before and after pre-straining are demonstrated in Fig. 2(i)−(l). For the sample without deformation, few dislocations are detected in the field of view (Fig. 2(i1)). Upon further straining, dislocation multiplications along {111} slip planes and interactions with microstructural features, such as dislocations, grain boundaries and carbides are clearly revealed (Fig. 2(j1)−(l1)). In some cases, cracked carbides are captured, as highlighted in Fig. 2(l). According to the SEM and STEM images, a statistical analysis of the dislocation density is plotted in Fig. 3(a). The

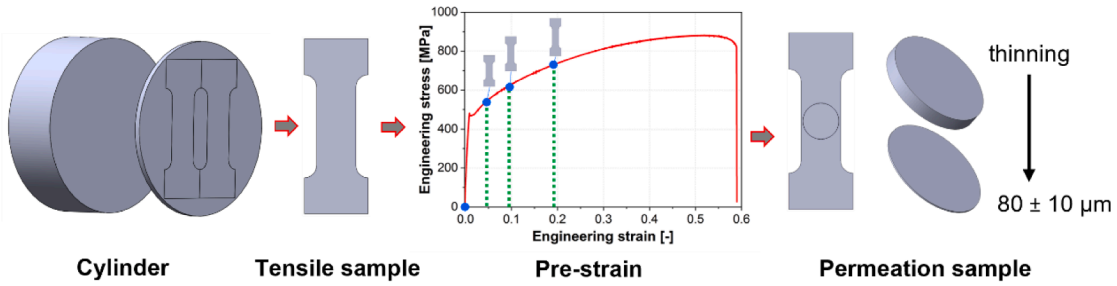

Fig. 1. Schematic of the sample preparation for electrochemical permeation test including the pre-straining, machining, and thinning processes.

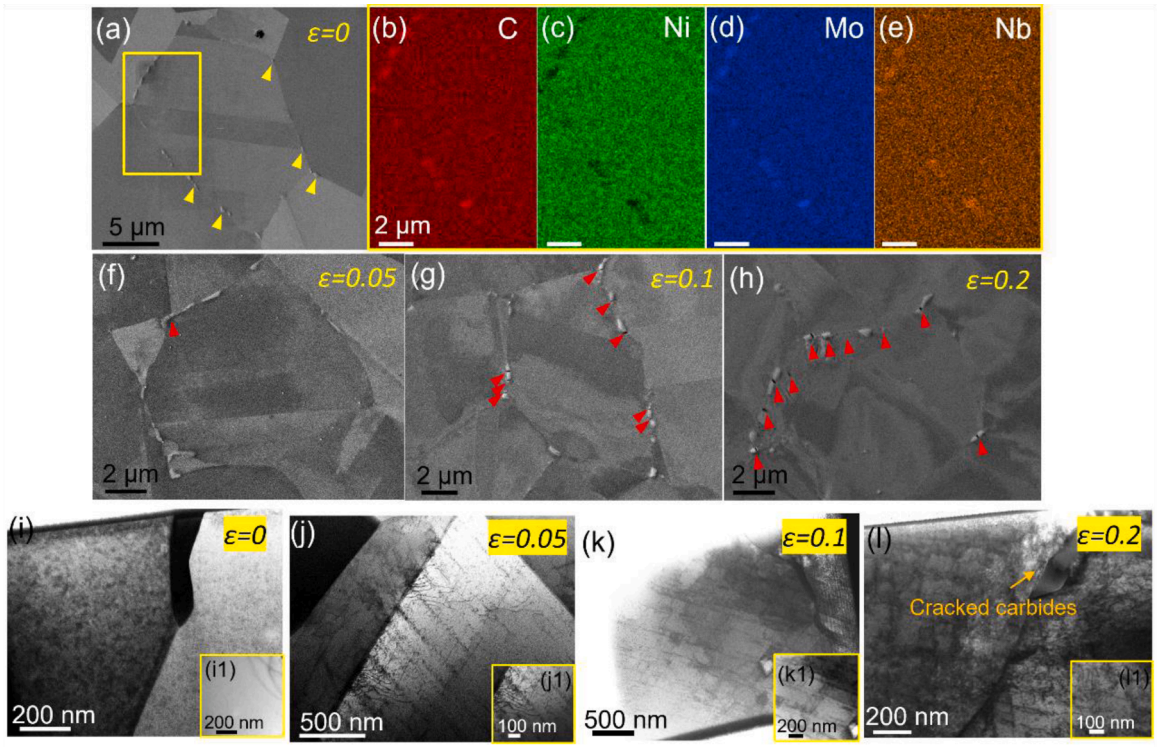

Fig. 2. (a) Micrograph of the pristine Alloy 625 sample showing secondary grain boundary precipitate; (b)–(e) EDS mapping of the highlighted area in (a) manifesting an enrichment of C, Mo, Nb and depletion of Ni in the precipitate; (f, g) micrographs of the samples at engineering strain of 0.1 and 0.2; (h) distribution of cracked carbide fraction under different loading conditions. (i)–(l) STEM images showing dislocations of the pristine sample and samples after pre-strain to 0.05,0.1, and 0.2.

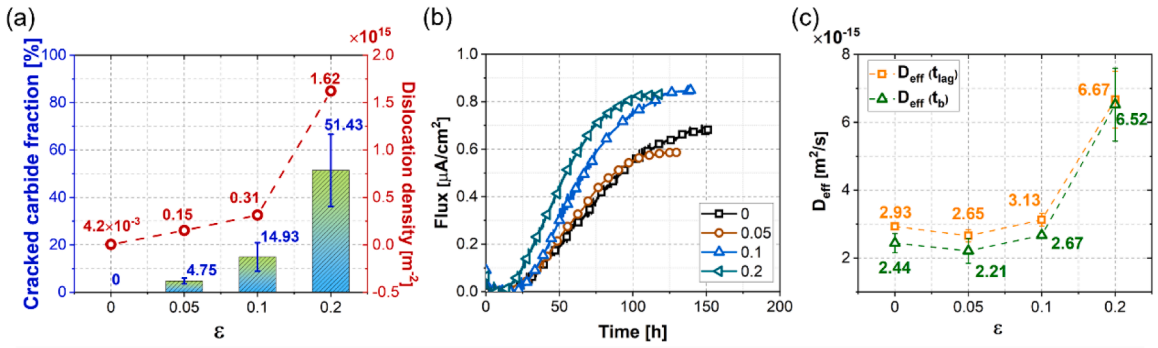

Fig. 3. (a) Statistical results of the cracked carbide fraction and dislocation density in the pristine microstructure and at different strains; (b) Hydrogen permeation flux and (c) the effective diffusion coefficients (D_{eff}) at strain levels of ε equals to 0, 0.05, 0.1 and 0.2.

dislocation density increases from 4.2×10^{12} m^{-2} in the pristine microstructure to 0.15×10^{15} and 0.31×10^{15} m^{-2} at strain 0.05 and 0.1. Furthermore, a pronounced dislocation multiplication at strain 0.2 with a density of 1.62×10^{15} m^{-2}, was observed. Additionally, based on the statistical analysis of about 300 carbides at each strain level, a summary of the cracked carbide fraction exhibits the same trend as that of the dislocation density (Fig. 3(a)). The number of cracked carbides increases with strain level. Specifically, 4.75% of the carbides were cracked at strain 0.05, and this fraction increases to 14.93% at strain 0.1. When the strain is increased to strain 0.2, more than half fraction of the total carbides were fractured. The microstructure evolution reflecting the permeation flux is presented in Fig. 3(b). The permeation curves show that the detection time for hydrogen remains approximately unchanged up to strain 0.1. What has been changed is the slope of the permeation curve, manifesting a change in both the hydrogen trapping and diffusion behavior. At the highest pre-strain condition (0.2), the hydrogen signal is detected in a much shorter time and the permeation slope is steeper. The escalated permeation gradient with pre-strain explicitly shows the attenuated hydrogen trapping in the microstructure.

In addition, the effective diffusion coefficient of hydrogen (D_{eff}) can be calculated by the time-lag (t_{lag}) and time-breakthrough (t_b) methods with the mathematical expressions derived from Fick's second law [36]:

$$D_{eff\left(t_{lag}\right)} = \frac{L^2}{6t_{lag}} \tag{7}$$

$$D_{eff(t_b)} = \frac{L^2}{15.3t_b} \tag{8}$$

where t_{lag} is the time (s) for the permeation flux to reach 0.63 of the steady-state current density i_∞. t_b is the breakthrough time that corresponds to 10% i_∞. L is the sample thickness (m). The results in Fig. 3(c)

shows a slight reduction in D_{eff} at strain 0.05 compared to the undeformed sample, while it further increases with strain exhibiting a drastic escalation, in particular, at strain 0.2.

Based on the aforementioned theory, an improved trapping model with grain boundary acceleration features considered was developed to assess the competition between the trapping and short-circuit diffusion at different strain levels. The permeation delay was numerically captured because N_d increases with the measured dislocation density; however, for a higher ϕ value, *i.e.,* for a higher D_{gb}, the grain boundaries serve as not only traps, but also fast diffusion pipes for hydrogen atoms, and this fact shifts j_{ss} by producing an earlier permeation transient. D_{eff} values were numerically obtained by a sweep study over different ϕ values and compared to the experimental values, using both the t_{lag} and t_b expressions, as shown in Fig. 4. In Fig. 4(a), each permeation transient is represented by a point ϕ (numerical input) and D_{eff} (fitted from the numerical output flux). The crossing point between numerical and experimental D_{eff} is expected to capture the real grain-boundary acceleration, *i.e.,* the ϕ value. Therefore, the fitted ϕ value depends on the D_{eff} fitting method (t_{lag} or t_b). It can be seen in Fig. 4(b) that even though the effective diffusivity obtained from numerical simulation fits the experimental value, the corresponding transient fluxes slightly deviate from the permeation tests. The simulated permeation transients for all the strain levels were plotted in Fig. 4(c, d) for both methods (t_{lag} and t_b). The observed deviation from experimental curves is attributed to the possible bias in the determination of D_L and energy values.

Despite the deviation, the influence of deformation on both the dislocation trapping and grain boundary acceleration was successfully captured and corroborated the experimental results. The increase in the fitted ϕ values with straining is plotted in Fig. 5 together with the cracked carbide fraction. As predicted by Turk et al. [31], the carbides originally act as obstacles to hydrogen diffusion along grain boundaries, and this phenomenon has been proven by the authors in a previous study on the non-deformed Alloy 625 by combining the hot extraction and

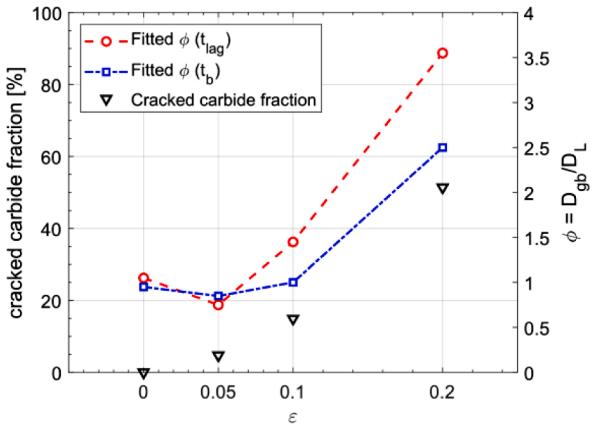

Fig. 5. Fitted ϕ values as a function of strain, with the cracked carbide fraction included.

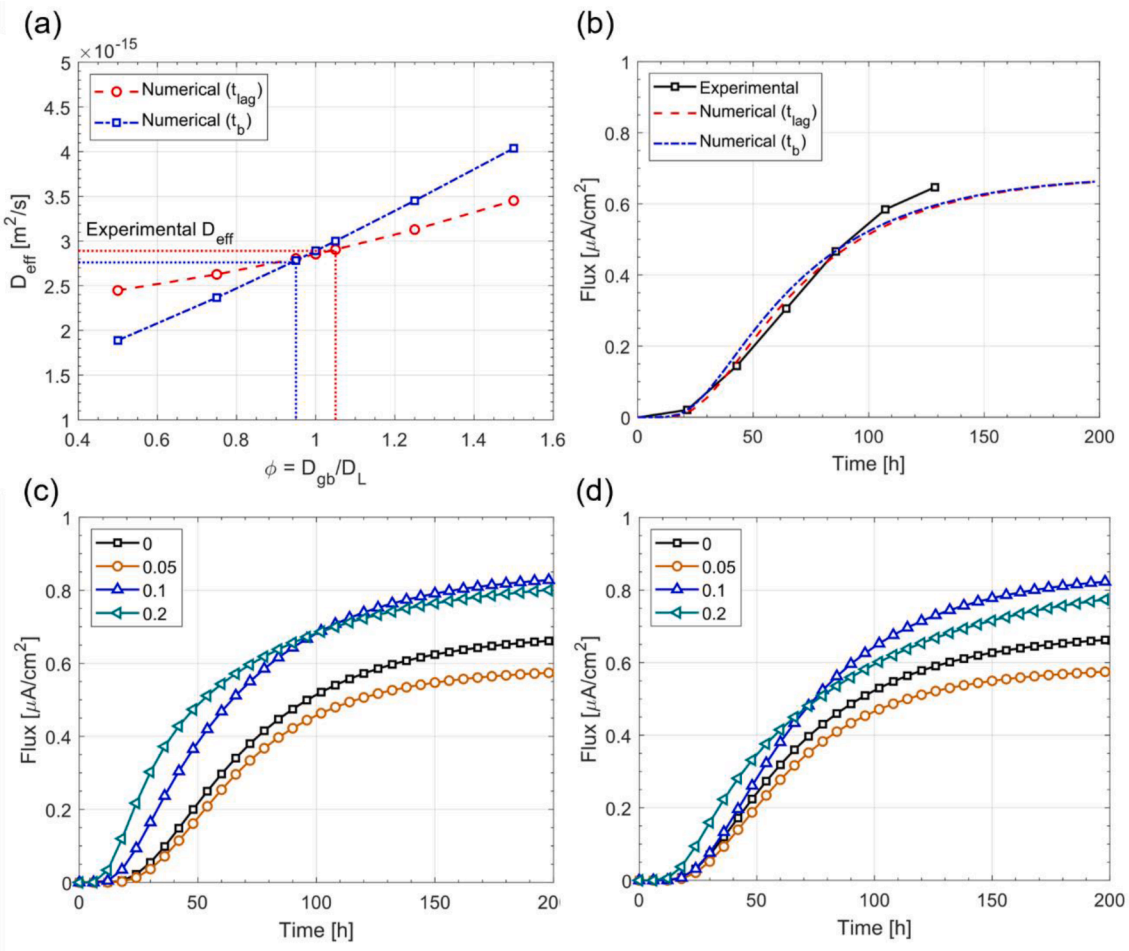

Fig. 4. Determination of ϕ for the unstrained condition using parametric sweep study; D_{eff} is obtained for different input ϕ values by fitting the simulated output flux. (a) Evolution of D_{eff} as a function of ϕ and compare with the experimental values, the crossing point (experimental-numerical) gives the estimation of ϕ; (b) Numerical permeation flux fitted to the experimental curve. Numerical permeation flux for ϕ values fitted from (c) t_{lag} (d) t_b at strain levels of 0, 0.05, 0.1, and 0.2.

thermal desorption analysis [37]. In that study, the sample with a higher fraction of grain boundary carbides demonstrated a lower D_{eff} and a lower absorbed hydrogen content after 45 h of charging, where the hydrogen concentration was far from the saturation level. In the case of pre-strain at 0.05, the slight decrease in D_{eff} is consistent with previous studies [23,26,27,31] demonstrating the effect of grain boundary carbides and reversible traps, here dislocations. However, we observed that even though the hydrogen diffusivity can be lowered because of the presence of carbides and the multiplication of reversible traps, when these carbides are progressively cracked as the sample was deformed to strain 0.1 and more, an acceleration in D_{gb} was confirmed from both the permeation results and trap modelling. The postulated reasons for the enhanced D_{gb} can thus be summarized as two aspects in the following: firstly, at higher strain levels, distortion at the grain boundaries and incoherent carbide interfaces are accommodated by strain-induced vacancy, which provide diffusion highways for hydrogen atoms that have been documented in previous studies [29,38,39]. Concomitantly, hydrogen atoms promote the formation of vacancies and vacancy clusters and further speed up the fast diffusion of hydrogen atoms along grain boundaries. Second, the removal of carbide interfaces during plastic deformation significantly reduces hydrogen trapping ability and contributes to the acceleration of hydrogen diffusion. Because carbides account for only 9.5% of the total grain boundary length, the effect of the cracked carbides and formation of micro-voids on hydrogen diffusivity is minor compared to the above reasons. Although the carbides potentially act as hydrogen traps, this effect seems to be overruled by the accelerating factors. This novel finding is at odds with previous observations and conveys important information regarding the validation of using existing diffusion equations to evaluate hydrogen mobility under plastic deformation pertaining to complex microstructures evolutions.

In conclusion, this is a first-hand study that correlates the hydrogen permeation behavior with the evolution of microstructure, in particular grain boundary carbide, under different pre-strain levels in a nickel Alloy 625. The results demonstrate an accelerated hydrogen diffusivity as the grain boundary carbides were cracked at strain higher than 0.1. As the multiplication of reversible traps (*i.e.,* dislocations) was claimed to reduce the diffusivity of hydrogen atoms, the acceleration in diffusivity was deduced to be caused by the diffusion highways by the hydrogen-enhanced strain-induced vacancies at the grain boundaries and reduced hydrogen trapping by the fractured carbides. The new insight of this study showcases that more attention should be devoted to the effect of deformation-induced microstructure evolution on hydrogen diffusion in materials, particularly for advanced alloys with precipitates at grain boundaries.

Declaration of Competing Interest

The authors declare that they have no known competing financial interests or personal relationships that could have appeared to influence the work reported in this paper.

Acknowledgments

The authors acknowledge the financial support from the Research Council of Norway through the project M-HEAT (294689) and the industry companies in the project. The Research Council of Norway is acknowledged for the support to the Norwegian Micro- and Nano-Fabrication Facility, NorFab, project number 295864. A. Díaz gratefully acknowledges the financial support from the Junta of Castile and Leon through grant BU-002-P20, co-financed by FEDER funds, and wishes to thank the Nanomechanical Lab of NTNU for providing hospitality during his research stay.

References

[1] A.M. Brass, J. Chene, Influence of deformation on the hydrogen behavior in iron and nickel base alloys: a review of experimental data, Mater. Sci. Eng. A 242 (1-2) (1998) 210–221.
[2] T. Cassagne, H. Marchebois, T. Mesquita, A review of hydrogen embrittlement of nickel-based alloys for oil and gas applications, Corrosion (2021), 16705.
[3] P.D. Hicks, C.J. Altstetter, Internal hydrogen effects on tensile properties of iron-base and nickel-base superalloys, Metall. Mater. Trans. A Phys. Metall. Mater. Sci. 21 (2) (1990) 365–372.
[4] A. Kimura, H.K. Birnbaum, Hydrogen induced grain-boundary fracture in high-purity nickel and its alloys - enhanced hydrogen diffusion along grain-boundaries, Acta Metall. 36 (3) (1988) 757–766.
[5] H. Sarmiento Klapper, J. Klöwer, O. Gosheva, Hydrogen embrittlement: the game changing factor in the applicability of nickel alloys in oilfield technology, Philos. Trans. R. Soc. 375 (2098) (2017), 20160415.
[6] Y. Yao, X.L. Pang, K.W. Gao, Investigation on hydrogen induced cracking behaviors of Ni-base alloy, Int. J. Hydrog. Energy 36 (9) (2011) 5729–5738.
[7] Z. Zhang, G. Obasi, R. Morana, M. Preuss, Hydrogen assisted crack initiation and propagation in a nickel-based superalloy, Acta Mater. 113 (2016) 272–283.
[8] Floreen, S.; Fuchs, G.E. and Yang, W.J., The Metallurgy of Alloy 625, Proceedings on Superalloys 718, 625, 706 and derivatives, E.A. Loria, Ed., The Minerals, Metals & Materials Society, (1994) 13–37.
[9] M.S. Hazarabedian, M.Z. Quadir, M. Iannuzzi, Characterization of intergranular phases in precipitation hardening Ni alloy UNS N07725, Mater. Charact. 171 (2021) 110770.
[10] R. Krakow, D.N. Johnstone, A.S. Eggeman, D. Hunert, M.C. Hardy, C.M.F. Rae, P. A. Midgley, On the crystallography and composition of topologically close-packed phases in ATI 718Plus (R), Acta Mater. 130 (2017) 271–280.
[11] L.F. Liu, K. Tanaka, A. Hirose, K.F. Kobayashi, Effects of precipitation phases on the hydrogen embrittlement sensitivity of Inconel 718, Sci. Technol. Adv. Mater. 3 (4) (2002) 335–344.
[12] M.S. Hazarabedian, M. Iannuzzi, The role of nano-sized intergranular phases on nickel alloy 725 brittle failure, NPJ Mater. Degrad. 5 (1) (2021).
[13] X. Lu, Y. Ma, D. Wang, On the hydrogen embrittlement behavior of nickel-based alloys: alloys 718 and 725, Mater. Sci. Eng. A 792 (2020) 139785.
[14] S. Frappart, X. Feaugas, J. Creus, F. Thebault, L. Delattre, H. Marchebois, Study of the hydrogen diffusion and segregation into Fe-C-Mo martensitic HSLA steel using electrochemical permeation test, J. Phys. Chem. Solids 71 (10) (2010) 1467–1479.
[15] H. Husby, M. Iannuzzi, R. Johnsen, M. Kappes, A. Barnoush, Effect of nickel on hydrogen permeation in ferritic/pearlitic low alloy steels, Int. J. Hydrog. Energy 43 (7) (2018) 3845–3861.
[16] J. Lee, C. Park, H. Park, N. Kang, Effective hydrogen diffusion coefficient for CoCrFeMnNi high-entropy alloy and microstructural behaviors after hydrogen permeation, Int. J. Hydrog. Energy 45 (16) (2020) 10227–10232.
[17] A. Oudriss, J. Creus, J. Bouhattate, C. Savall, B. Peraudeau, X. Feaugas, The diffusion and trapping of hydrogen along the grain boundaries in polycrystalline nickel, Scr. Mater. 66 (1) (2012) 37–40.
[18] J. Xu, X.K. Sun, Q.Q. Liu, W.X. Chen, Hydrogen permeation behavior in In718 and Gh761 superalloys,, Metall. Mater. Trans. A Phys. Metall. Mater. Sci. 25 (3) (1994) 539–544.
[19] T. Zakroczymski, Adaptation of the electrochemical permeation technique for studying entry, transport and trapping of hydrogen in metals, Electrochim. Acta 51 (11) (2006) 2261–2266.
[20] T.M. Zhang, W.M. Zhao, T.T. Li, Y.J. Zhao, Q.S. Deng, Y. Wang, W.C. Jiang, Comparison of hydrogen embrittlement susceptibility of three cathodic protected subsea pipeline steels from a point of view of hydrogen permeation, Corros. Sci. 131 (2018) 104–115.
[21] P.W. Zhou, W. Li, H.S. Zhao, X.J. Jin, Role of microstructure on electrochemical hydrogen permeation properties in advanced high strength steels, Int. J. Hydrog. Energy 43 (24) (2018) 10905–10914.
[22] K.S. de Assis, C.G.C. Schuabb, M.A. Lage, M.P.P. Gonçalves, D.P. Dias, O.R. Mattos, Slow strain rate tests coupled with hydrogen permeation: new possibilities to assess the role of hydrogen in stress corrosion cracking tests part I: methodology and commissioning results, Corros. Sci. 152 (2019) 45–53.
[23] S.J. Kim, D.W. Yun, D.W. Suh, K.Y. Kim, Electrochemical hydrogen permeation measurement through TRIP steel under loading condition of phase transition, Electrochem. Commun. 24 (2012) 112–115.
[24] D. Sun, M. Wu, F. Xie, K. Gong, Hydrogen permeation behavior of X70 pipeline steel simultaneously affected by tensile stress and sulfate-reducing bacteria, Int. J. Hydrog. Energy 44 (43) (2019) 24065–24074.
[25] E. Van den Eeckhout, I. De Baere, T. Depover, K. Verbeken, The effect of a constant tensile load on the hydrogen diffusivity in dual phase steel by electrochemical permeation experiments, Mater. Sci. Eng. A 773 (2020), 138872.
[26] W. Zhao, T. Zhang, Z. He, J. Sun, Y. Wang, Determination of the critical plastic strain-induced stress of X80 steel through an electrochemical hydrogen permeation method, Electrochim. Acta 214 (2016) 336–344.
[27] S.J. Kim, K.Y. Kim, Electrochemical hydrogen permeation measurement through high-strength steel under uniaxial tensile stress in plastic range, Scr. Mater. 66 (12) (2012) 1069–1072.
[28] X. Lu, D. Wang, R. Johnsen, Hydrogen diffusion and trapping in nickel-based Alloy 625: an electrochemical permeation study, Electrochim. Acta 421 (2022), 140477.
[29] A. Oudriss, J. Creus, J. Bouhattate, E. Conforto, C. Berziou, C. Savall, X. Feaugas, Grain size and grain-boundary effects on diffusion and trapping of hydrogen in pure nickel, Acta Mater. 60 (19) (2012) 6814–6828.

[30] P. Sofronis, R.M. McMeeking, Numerical analysis of hydrogen transport near a blunting crack tip, J. Mech. Phys. Solids 37 (3) (1989) 317–350.
[31] A. Turk, D. Bombač, J. Jelita Rydel, M. Zięćara, P.E.J. Rivera-Díaz-del-Castillo, E. I. Galindo-Nava, Grain boundary carbides as hydrogen diffusion barrier in a Fe-Ni alloy: a thermal desorption and modelling study, Mater. Des. 160 (2018) 985–998.
[32] M. Dadfarnia, P. Sofronis, T. Neeraj, Hydrogen interaction with multiple traps: can it be used to mitigate embrittlement? Int. J. Hydrog. Energy 36 (16) (2011) 10141–10148.
[33] E. Torres, J. Pencer, D.D. Radford, Atomistic simulation study of the hydrogen diffusion in nickel, Comput. Mater. Sci. 152 (2018) 374–380.
[34] T. Zirkle, L. Costello, T. Zhu, D.L. McDowell, Modeling dislocation-mediated hydrogen transport and trapping in face-centered cubic metals, J. Eng. Mater. Technol. 144 (1) (2021), 011005.
[35] Y. Meng, X. Ju, X. Yang, The measurement of the dislocation density using TEM, Mater. Charact. 175 (2021), 111065.
[36] M.A.V. Devanathan, Z. Stachurski, F.C. Tompkins, The adsorption and diffusion of electrolytic hydrogen in palladium, Proc. R. Soc. A Math. Phys. Eng. Sci. 270 (1340) (1962) 90–102.
[37] X. Lu, T. Depover, R. Johnsen, Evaluation of hydrogen diffusion and trapping in nickel Alloy 625 by thermal desorption spectroscopy, Int. J. Hydrog. Energy 47 (74) (2022) 31673–31683.
[38] J. Li, A. Hallil, A. Metsue, A. Oudriss, J. Bouhattate, X. Feaugas, Antagonist effects of grain boundaries between the trapping process and the fast diffusion path in nickel bicrystals, Sci. Rep. 11 (1) (2021) 15533.
[39] A. Metsue, A. Oudriss, X. Feaugas, Hydrogen solubility and vacancy concentration in nickel single crystals at thermal equilibrium: new insights from statistical mechanics and ab initio calculations, J. Alloy. Compd. 656 (2016) 555–567.